

**Robust platform for engineering pure-quantum-state transitions in polariton condensates**A. Askitopoulos,<sup>1,\*</sup> T. C. H. Liew,<sup>2</sup> H. Ohadi,<sup>1,†</sup> Z. Hatzopoulos,<sup>3,4</sup> P. G. Savvidis,<sup>3,5</sup> and P. G. Lagoudakis<sup>1</sup><sup>1</sup>*Faculty of Physical Sciences and Engineering, University of Southampton, Southampton SO17 1BJ, United Kingdom*<sup>2</sup>*School of Physical and Mathematical Sciences, Nanyang Technological University, 637371 Singapore*<sup>3</sup>*Microelectronics Research Group, IESL-FORTH, P.O. Box 1527, 71110 Heraklion, Crete, Greece*<sup>4</sup>*Department of Physics, University of Crete, 71003 Heraklion, Crete, Greece*<sup>5</sup>*Department of Materials Science and Technology, University of Crete, Crete, Greece*

(Received 18 November 2014; revised manuscript received 19 May 2015; published 16 July 2015)

We report on pure-quantum-state polariton condensates in optical annular traps. The study of the underlying mechanism reveals that the polariton wave function always coalesces in a single pure quantum state that, counterintuitively, is always the uppermost confined state with the highest overlap with the exciton reservoir. The tunability of such states combined with the short polariton lifetime allows for ultrafast transitions between coherent mesoscopic wave functions of distinctly different symmetries, rendering optically confined polariton condensates a promising platform for applications such as many-body quantum circuitry and continuous-variable quantum processing.

DOI: [10.1103/PhysRevB.92.035305](https://doi.org/10.1103/PhysRevB.92.035305)

PACS number(s): 71.36.+c, 03.75.Kk, 71.35.Lk

Polaritons in semiconductor microcavities are light-matter bosonic quasiparticles formed by strong coupling of cavity photons and intracavity excitons [1]. Their excitonic part gives rise to strong interactions essential for fast thermalization and condensation, while their photonic part contributes to their very low effective mass ( $5 \times 10^{-5} m_e$ ), allowing for high-temperature condensation [2]. Polariton condensates have been observed both under nonresonant optical excitation [3] and more recently under electrical injection of carriers [4,5]. However, polaritons populate a two-dimensional plane where a true Bose phase transition is theoretically possible only in the presence of a confining potential [6], and this was first demonstrated with a stress-induced trap [7]. Unlike the weak atom-atom interactions in cold atomic Bose-Einstein condensates (BECs), interparticle interactions in a semiconductor microcavity are strong enough to substantially renormalize polariton self-energy, experimentally observed as a local blueshift of the polariton spectrum. Variations of the polariton density in the plane of the cavity result in a potential landscape that can be externally controlled through real-space modulation of the optical excitation beam. The malleability of the potential landscape can be used to imprint scattering centers [8] and devise polariton traps [9,10] and gates [11]. The dynamics of polariton condensates in externally modulated potential landscapes can lead to trapped states, standing polariton waves, and phase locking of remote condensates in nontrivial configurations [9,12–16]. Extensive control over mesoscopic polariton wave functions and their transitions between quantum states, coupled with the extensive propagation of polaritonic flows [8,17], leads to applications in quantum control, quantum circuits, and on-chip quantum information processing [18,19].

In this paper, we investigate the dynamics of pure quantum state transitions of polariton condensates under optical confinement. We utilize a ring-shaped, nonresonant optical

excitation scheme to create a size-tunable annular potential trap. Under continuous-wave excitation, we study the steady-state regime of trapping and condensate formation. We control the height of the potential trap by tuning the optical excitation density and observe that, at coherence threshold, polaritons coalesce preferentially at the uppermost confined energy state that has the largest wave function overlap with the exciton reservoir that forms the trap barriers. To confirm that excited-state polariton condensates are realized predominantly by polariton confinement in the optically induced potential trap, we study the transient dynamics of the formation mechanism. For this purpose, we change from continuous-wave to pulsed excitation, while keeping all other parameters unaltered, and time-resolve the evolution of the spatial polariton state. Under pulsed excitation, the height of the potential barrier is transiently diminishing following the decay of the exciton reservoir. We observe that the mesoscopic polariton condensate switches between states, progressively transforming to the highest available confined energy state. The experimental observations are accurately reproduced using the extended Gross-Pitaevski equation.

Non-ground-state condensates of spatially confined polaritons were previously observed in optical defect sites and in pillar microcavities, under Gaussian-shaped nonresonant optical excitation incident to the confinement area [20–22]. While gain competition in thermodynamic equilibrium has been predicted to give rise to occupation of a single or several excited states [23,24], in both cases, excited-state condensates were shown to be driven by the dynamics of energy relaxation across the confined energy states, resulting in multistate condensation. In the case of ring-shaped excitation, two characteristically different regimes of polariton condensates have been realized. For ring radii comparable to the thermal de-Broglie wavelength, a phase-locked standing-wave condensate colocalized with the excitation area was observed [12]. For ring radii comparable to the polariton propagation length in the plane of the cavity, the excitation ring acted as a potential barrier and a Gaussian-shaped ground-state polariton condensate was realized [9]. Christofolini and co-workers examined the transition between phase-locked and trapped condensates using

\*Corresponding author: alexis.askitopoulos@soton.ac.uk

†Current address: Department of Physics, Cavendish Laboratory, University of Cambridge, Cambridge CB3 0HE, United Kingdom.

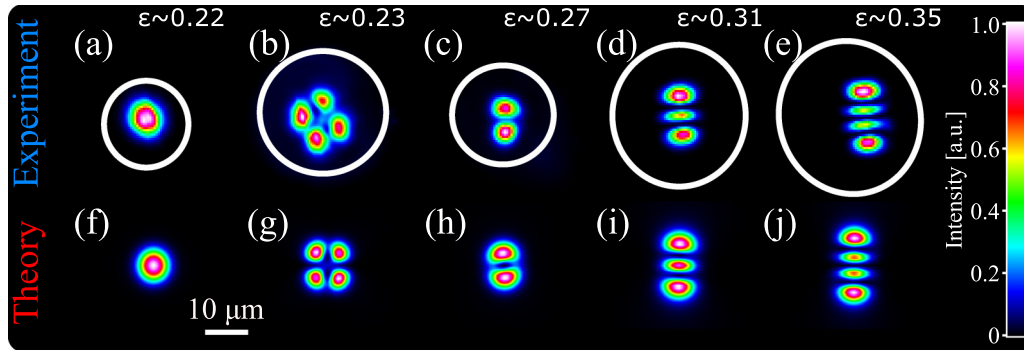


FIG. 1. (Color online) False color-scale experimental (a)–(e) and theoretical (f)–(j) states of polariton condensates. (a),(f)  $\Psi_{00}$ , (b),(g)  $\Psi_{11}$ , (c),(h)  $\Psi_{01}$ , (d),(i)  $\Psi_{02}$ , and (e),(j)  $\Psi_{03}$ .  $\epsilon$  denotes the ellipticity of individual configurations.

multiple-excitation spots and a ring-shaped excitation pattern [13]. Despite earlier work by Manni *et al.* [12], the authors claimed that, for ring-shaped pumps, no phase-locked state is geometrically possible, and that when the spacing between the pumps is reduced, the trapped condensate collapses into a Gaussian-shaped ground state. Here, we show that under ring-shaped excitation, the formation of excited-state condensates is driven by polariton confinement in the linear potentials and that the presence of non-ground-state polariton condensates does not necessitate asymmetries in the shape and/or power distribution of the ring excitation. The dependence of the state selection on the height of the trap's barrier and shape at threshold provides a robust platform for engineering switches of mesoscopic multiparticle coherent states.

The experimental configuration that produces an annular beam of zero angular momenta consists of a double-axicon arrangement. A variable telescope is used to control the radii of the excitation beam that we project on the sample. The excitation and detection configuration and the microcavity sample are described in Ref. [9]. The microcavity is held in a cold finger cryostat operating at 6 K. We study the steady-state dynamics under nonresonant excitation at 752 nm using a single-mode quasi-continuous-wave (cw) laser (2% on-off ratio at 10 kHz). The microcavity used in these experiments is a high- $Q$ -factor ( $>15\,000$ )  $5\lambda/2$  GaAs/AlGaAs microcavity with four triplets of 10 nm GaAs quantum wells, with a Rabi splitting of 9 meV and a cavity lifetime of 7 ps, as described in Ref. [25]. All experiments were performed for a small negative detuning range of  $-7 \leq d \leq -5$  meV.

Figures 1(a)–1(e) show the spatial profiles of mesoscopic wave functions for a range of excitation radii and asymmetries, characterized by the ellipticity and radius of the excitation ring, at the coherence threshold that defines the depth of the trap via the interactions in the reservoir. These states resemble the TEM modes of a harmonic oscillator, and in what follows we will adapt their symbolism to annotate the state of the polariton wave function. For an excitation ring with a radius of  $\sim 10\ \mu\text{m}$  we observe a ground-state polariton condensate [Fig. 1(a)], as in Ref. [9], which remains in the ground state as long as the long axis of the asymmetric excitation does not exceed  $\sim 10\ \mu\text{m}$ . For larger excitation ring radius ( $\sim 17\ \mu\text{m}$ ) and similar ellipticity as in Fig. 1(a) ( $\epsilon = 0.22$ ) at the coherence threshold we observe that polaritons coalesce at a higher excited state ( $\psi_{11}$ ) as shown in Fig. 1(b). We note that

the symmetry of the excited-state wave function is robust to small asymmetries in the excitation ring ( $0 < \epsilon < 0.23$ ) and the transition from ground to nonground polariton condensates is predominantly dependent on the radius of the ring. By increasing the ring radius and the asymmetry of the excitation, it is possible to observe excited-state polariton condensates as shown in Figs. 1(a)–1(c). On top of each panel we have annotated the ellipticity of the excitation ring. Interferometric measurements of the excited states  $\psi_{01}$ ,  $\psi_{02}$ , and  $\psi_{03}$  confirm that these are coherent mesoscopic wave functions of extended condensates [Figs. 2(a)–2(c)].

We investigate the dependence of the quantum-state selectivity on the barrier height by varying the nonresonant excitation density of a geometrically fixed, ring-shaped, asymmetric excitation profile. We use an excitation ring of radius  $\sim 16\ \mu\text{m}$  and  $\epsilon = 0.27$  that at coherence threshold produces the  $\Psi_{04}$  polariton state as shown in Fig. 3(a). By increasing the excitation density above the coherence threshold, while keeping all other parameters the same, we observe the transition from  $\Psi_{04}$  to  $\Psi_{05}$  [Fig. 3(b)]. The order of the latter state is clearly revealed in Fig. 3(c), where we plot the normalized spatial profiles along the white dashed lines of the real-space intensity images of Figs. 3(a) and 3(b). Figure 3(c) shows the presence of an extra node at the higher excitation density indicative of  $\Psi_{05}$ . In Fig. 3(d) we plot the energy shift of the condensate in the transition from  $\Psi_{04}$  to  $\Psi_{05}$  with respect to its energy at the coherence threshold [ $\Delta(E_P - E_{P_{\text{th}}})$ ]. A sharp increase of the energy shift ( $\sim 45\ \mu\text{eV}$ ) is observed in Fig. 3(d) at  $P \sim 1.12P_{\text{th}}$ . Within the gray stripe intensity fluctuations of the excitation beam artificially blur the two states. The top panels in Figs. 3(a) and

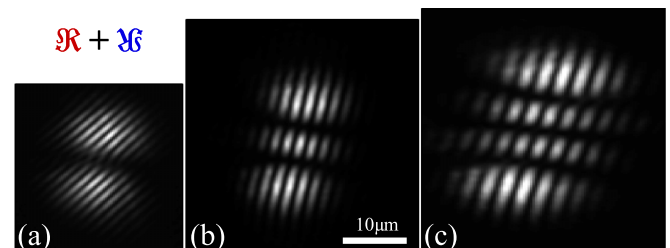


FIG. 2. (Color online) Interference patterns of trapped polariton condensates: (a)  $\Psi_{01}$ , (b)  $\Psi_{02}$ , and (c)  $\Psi_{03}$ . The interference patterns were obtained with a retroreflector configuration.

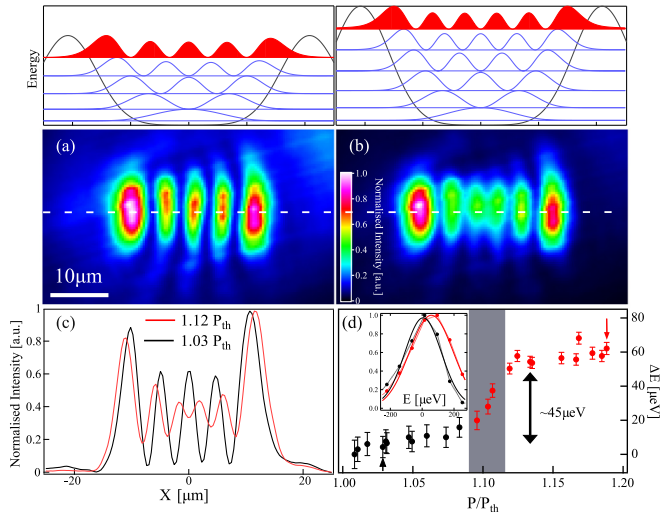


FIG. 3. (Color online) Evolution of  $\Psi_{04}$  for increasing excitation density. Bottom panel: (a)  $\Psi_{04}$  at  $P = 1.03P_{th}$ . (b) Subsequent increase of the power results at the appearance of  $\Psi_{05}$ . Top panel: Schematic representation of the confined energy states for two different barrier heights. (c) Profiles of the wave function for different excitation densities extracted along the dashed white lines in (a) and (b). (d) Corresponding energy difference with respect to the energy at the coherence threshold for increasing excitation power normalized at the coherence threshold power  $P_{th}$ . Inset in (d) shows the spectra of the points denoted by the arrows.

3(b) depict the calculated energy levels for the trap shape and the corresponding probability density of the confined states. In both panels, the red-filled probability density corresponds to the occupied state. It is worth noting here the greater overlap of the probability density of the highest energy level [ $\Psi_{04}$  in Fig. 3(a) and  $\Psi_{05}$  in Fig. 3(b)] with the reservoir compared to the lowest energy levels. Evidently, with increasing barrier height a polariton condensate is realized at the next confined energy level as a pure quantum state that can be singularly described by the principal quantum number  $n$  ( $\Psi_{0,n+1}$ ).

We explore the robustness of the formation of pure quantum states against density fluctuations in the exciton reservoir, by extending our study from the excitation-density-dependent switching between successive states in the dynamic equilibrium regime to transitions in the time domain under nonresonant pulsed excitation. We use a ring-shaped nonresonant 200 fs pulse at 755 nm with  $\sim 11 \mu\text{m}$  radius of the major axis and  $\epsilon = 0.3$  at  $\sim 1.6P_{th}$ . We record the spatiotemporal dynamics of the emission and observe the formation of the  $\Psi_{01}$  polariton state and its transition to  $\Psi_{00}$  [26]. We set the transition point to define the zero time frame for the rest of our analysis. Figure 4(a) shows a snapshot of the  $\Psi_{01}$  state at  $-30$  ps. At later times, the two lobes of the  $\Psi_{01}$  state appear to move closer together, and the condensate rapidly transforms to the ground polariton state ( $\Psi_{00}$ ) of Fig. 4(b). The decrease of the density in the barriers in the time domain results in a shallower trap in which the  $\Psi_{01}$  state is no longer confined, leading to a polariton condensate at the next available state, here the ground state  $\Psi_{00}$ . We spectrally and

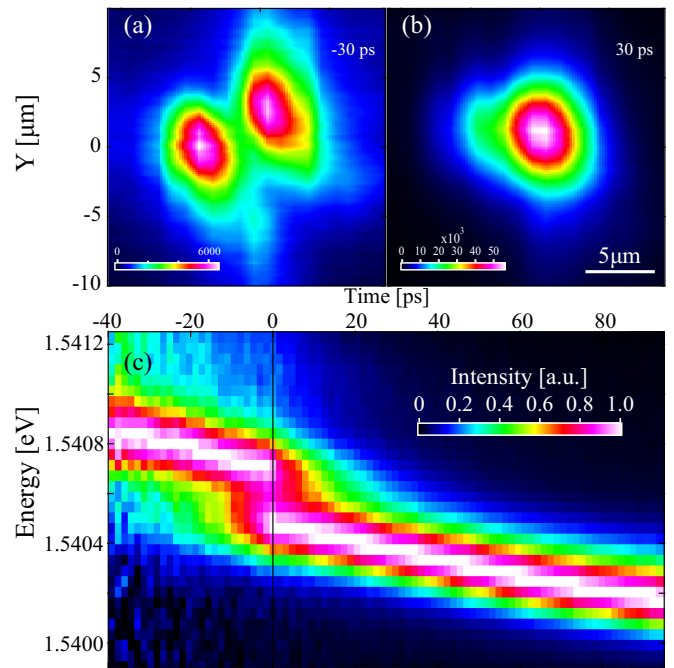


FIG. 4. (Color online) False color-scale real-space tomographic frames in the time domain. (a)  $\Psi_{01}$  state at  $-30$  ps and (b) subsequent transition to  $\Psi_{00}$  at 30 ps. (c) Intensity-normalized time evolution of the emission energy showing the characteristic energy jump at the transition threshold.

time-resolve the decay of emission at normal incidence with an angular width corresponding to  $|k| \leq 1.4 \mu\text{m}$  and observe a sharp energy shift from  $\Psi_{01}$  to  $\Psi_{00}$  as shown in Fig. 4(c). This dynamic transition further illustrates that under optical confinement a polariton condensate spontaneously occurs at a higher confined state as defined by the barrier height of the trap, and that the transition to the ground state is hindered solely by the existence of higher energy levels.

The time-resolved dispersion images from which the energy evolution of the system was extracted [Fig. 4(c)] are presented in Figs. 5(a)–5(c). The appearance of the  $\Psi_{01}$  mode is accompanied by a distinct doublet mode in the dispersion [Fig. 5(a)], which corresponds to the counterpropagating components of the standing wave [14]. As the barrier dynamically decays and the  $\Psi_{00}$  mode is switched on as previously discussed, it quickly overtakes  $\Psi_{01}$  in intensity at  $\sim 0$  ps. The first excited state quickly dissipates after this point with the polariton lifetime, and the dispersion is dominated by the emission of the trap ground state. Interestingly, Figs. 5(a)–5(c) also reveal distinct satellite modes at the same energy of the confined modes but for greater in-plane wave vector. For quantum states in traps with a finite barrier width, coherent tunneling modes are a characteristic feature. Moreover, in our system these modes will be accelerated by the potential landscape outside the trap eventually acquiring momentum characteristic of the difference between the energy level in the trap and of the low-density polariton dispersion of the system outside the excitation region [Fig. 5(d)]. From this description it becomes clear that the tunneling modes are expected to be

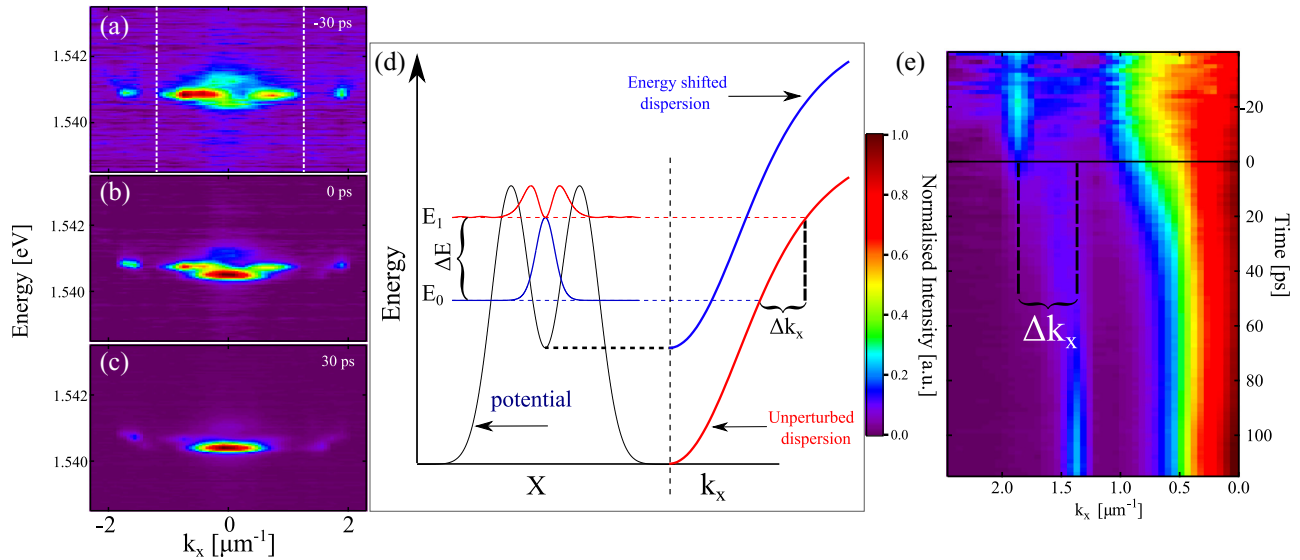


FIG. 5. (Color online) Polariton dispersion at  $-30$  ps (a),  $0$  ps, (b), and  $30$  ps (c). White dotted lines in (a) denote the integrated area from which Fig. 4(c) was extracted. (d) Schematic representation of the momentum acquired by polaritons tunneling outside the potential trap (potential and dispersion energy not in scale). (e) Intensity-normalized time evolution of  $k_x$ , showing the characteristic  $\Delta k_x$  jump of the tunneling mode.

at the same energy but with higher momentum, as observed in Figs. 5(a)–5(c).

Integrating the time-dispersion images over energy, while intensity-normalizing for every time frame, we compile the time evolution of  $k_x$  [Fig. 5(e)]. This analysis reveals the expected  $\Delta k_x$  difference of the tunneling modes of the two states. Intuitively, the relative (to the trapped state) intensity of the  $\Psi_{01}$  tunneling mode at the transition is substantial, as the width of the barrier goes to zero at this energy level. In contrast to the tunneling amplitude of the ground state which is effectively suppressed as the potential width at the  $\Psi_{01}$  energy level is still significant. Nevertheless, following the dynamic dissipation of the barrier, due to the decay of particles as well as draining of the reservoir by the condensate, we observe a continuous increase of the relative intensity of the tunneling amplitude of the ground state at  $k_x \sim 1.4 \mu\text{m}^{-1}$ . The observation of a strong tunneling component from the  $E_{01}$  energy just before the transition verifies that the barrier width for this level is indeed minimal and that  $\Psi_{01}$  is close to the rim of the trap barrier, further corroborating our interpretation.

The system can be theoretically modeled with a nonlinear Schrödinger equation, namely, the Gross-Pitaevski equation. Simulations with the Gross-Pitaevski equation with a potential similar to the one from the experimental measurements in our system qualitatively reproduce the states recorded experimentally. Using a potential  $V(r)$  that consists of the exciton-exciton interactions in the reservoir, which blueshift the polariton energy levels, and of the polariton-polariton interactions in the condensate, the Hamiltonian of the system is

$$H(r) = T + V(r), \quad (1)$$

$$V(r) = V_r(r) + V_c(r), \quad (2)$$

$$V_r(r) = N_r U_{\text{ex-ex}} f_r(r), \quad (3)$$

where  $N_r$  is the density of excitons in the reservoir,  $U_{\text{ex-ex}}$  is the exciton-exciton interaction strength,  $f_r(\mathbf{r})$  is the spatial distribution of the exciton reservoir taking into account exciton diffusion beyond the pump spot, and  $V_c = U_{\text{pol-pol}} |\psi_n(\mathbf{r})|^2$  with  $U_{\text{pol-pol}}$  the polariton-polariton interaction strength and  $\psi(\mathbf{r})$  the condensate wave function. In addition to kinetic and potential energy terms in the above Hamiltonian, to account for polariton spatial dynamics, a generalization of the extended Gross-Pitaevskii equation is required to include incoherent pumping and decay [27]. In continuous-wave experiments one expects the excitation of a steady state of hot excitons with the spatial profile set by the optical pumping extended by exciton diffusion. One can then make use of the Landau-Ginzburg approach for describing the dynamics of the two-dimensional (2D) polariton wave function [28]:

$$\begin{aligned} i\hbar \frac{d\psi(\mathbf{r},t)}{dt} = & \left[ -\frac{\hbar^2 \hat{\nabla}^2}{2m_p} + (U_{\text{pol-pol}} - i\Gamma_{\text{NL}}) |\psi(\mathbf{r},t)|^2 \right. \\ & \left. + (U_{\text{pol-ex}} + ir) N_r f_r(\mathbf{r}) - \frac{i\Gamma}{2} \right] \psi(\mathbf{r},t) \\ & + i\hbar \mathfrak{R}[\psi(\mathbf{r},t)]. \end{aligned} \quad (4)$$

Here  $m_p$  is the polariton effective mass and  $f_r(\mathbf{r})$  describes the 2D spatial distribution of  $N_r$  excitons. The condensation rate  $r$  describes the gain of polaritons in the presence of the exciton reservoir. The polaritons experience both a linear decay  $\Gamma$  and nonlinear loss  $\Gamma_{\text{NL}}$ , which represents the scattering of polaritons out of the condensate when its density is high [28]. The final term in Eq. (4) represents a phenomenological energy relaxation [29] in the system, which can play an important role when non-ground-state polaritons interact with a potential gradient [30–32]:

$$\mathfrak{R}[\psi(x,t)] = -\lambda N_r f_r(\mathbf{r}) [\hat{E}_{\text{LP}} - \mu(\mathbf{r},t)] \psi(x,t), \quad (5)$$

where  $\lambda$  determines the strength of energy relaxation [29,31] and  $\mu(\mathbf{r}, t)$  is a local effective chemical potential that conserves the polariton population [29]. Kinetic energy relaxation of this form was derived with a variety of methods [33,34] and offers a simple model for the qualitative description of our experiment. We note, however, that this model does not distinguish between different mechanisms of energy relaxation, which may have different power dependences [35].

Fixing  $N_r$ ,  $f_r(\mathbf{r})$  to represent a ring-shaped excitation (with slight asymmetry), the numerical solution of Eq. (4) gives the steady-state intensity profiles shown in Figs. 1(f)–1(j). Different configurations are accessed by varying the spatial distribution [ $f_r(\mathbf{r})$ ] and population ( $N_r$ ) of hot excitons, as in the experiment [36]. The simulations support that excited-state condensation occurs preferentially at the uppermost confined energy state.

Although it cannot be explicitly verified that there is no available state in the trap above the condensate energy level, since the polariton potential landscape is not directly measurable, the evidence presented from the steady-state switching and the transient study including the dynamic behavior of the tunneling components of the system, as well as the theoretical simulations and the calculations for the condensate reservoir overlap [26], strongly supports our interpretation that polaritons condense in the highest available energy state within the optical trap.

In conclusion, we have investigated the dynamics of polariton condensates under optical confinement and observed that, in contrast to previously reported excited-state condensation in

defect traps and pillar structures, injection of polaritons from the trap barriers leads to the formation of a pure quantum-confined state with a mesoscopic coherent wave function above the condensation threshold. This behavior is in agreement with theoretical expectations for a true Bose condensate that is anticipated to resist multimode behavior [37,38] in the presence of interparticle interactions. Moreover, we revealed that the state selectivity of this system strongly depends on the geometric properties of the trap and have demonstrated a highly controllable switching between successive mesoscopic coherent quantum-confined states, in the dynamic equilibrium regime and in the time domain. These results highlight the capability of tailoring and manipulating on-chip pure quantum states in semiconductor microcavities that can facilitate the implementation of polariton bosonic cascade lasers [39]. Taking into account that the extensive propagation [38] as well as the susceptibility of the polaritonic flow to the potential landscape [40] have been widely demonstrated, these results also indicate the potential for engineering confined condensate lattices, coupled by their respective tunneling amplitudes. Moreover, the coupling strength in this architecture can be finely tuned by controlling the barrier height, enabling the emergence of applications such as many-body quantum circuitry and quantum simulators.

A.A. acknowledges useful discussions with W. Langbein and S. Portolan. P.S. acknowledges funding from Greek GSRT ARISTEIA program Apollo.

- 
- [1] H. Deng, H. Haug, and Y. Yamamoto, *Rev. Mod. Phys.* **82**, 1489 (2010).
- [2] S. Christopoulos, G. H. H. von Högersthal, A. Grundy, P. G. Lagoudakis, A. V. Kavokin, J. J. Baumberg, G. Christmann, R. Butte, E. Feltin, J.-F. Carlin, and N. Grandjean, *Phys. Rev. Lett.* **98**, 126405 (2007).
- [3] J. Kasprzak, M. Richard, S. Kundermann, A. Baas, P. Jembrun, J. M. J. Keeling, F. M. Marchetti, M. H. Szymańska, R. André, J. L. Staehli, V. Savona, P. B. Littlewood, B. Deveaud, and L. S. Dang, *Nature (London)* **443**, 409 (2006).
- [4] C. Schneider, A. Rahimi-Iman, N. Y. Kim, J. Fischer, I. G. Savenko, M. Amthor, M. Lerner, A. Wolf, L. Worschech, V. D. Kulakovskii, I. A. Shelykh, M. Kamp, S. Reitzenstein, A. Forchel, Y. Yamamoto, and S. Höfling, *Nature (London)* **497**, 348 (2013).
- [5] P. Bhattacharya, B. Xiao, A. Das, S. Bhowmick, and J. Heo, *Phys. Rev. Lett.* **110**, 206403 (2013).
- [6] O. L. Berman, Y. E. Lozovik, and D. W. Snoke, *Phys. Rev. B* **77**, 155317 (2008).
- [7] R. Balili, V. Hartwell, D. Snoke, L. Pfeiffer, and K. West, *Science* **316**, 1007 (2007).
- [8] D. Sanvitto, S. Pigeon, A. Amo, D. Ballarini, M. D. Giorgi, I. Carusotto, R. Hivet, F. Pisanello, V. G. Sala, P. S. S. Guimaraes, R. Houdré, E. Giacobino, C. Ciuti, A. Bramati, and G. Gigli, *Nat. Photonics* **5**, 610 (2011).
- [9] A. Askitopoulos, H. Ohadi, A. V. Kavokin, Z. Hatzopoulos, P. G. Savvidis, and P. G. Lagoudakis, *Phys. Rev. B* **88**, 041308 (2013).
- [10] R. Dall, M. D. Fraser, A. S. Desyatnikov, G. Li, S. Brodbeck, M. Kamp, C. Schneider, S. Höfling, and E. A. Ostrovskaya, *Phys. Rev. Lett.* **113**, 200404 (2014).
- [11] T. Gao, P. S. Eldridge, T. C. H. Liew, S. I. Tsintzos, G. Stavrinidis, G. Deligeorgis, Z. Hatzopoulos, and P. G. Savvidis, *Phys. Rev. B* **85**, 235102 (2012).
- [12] F. Manni, K. G. Lagoudakis, T. C. H. Liew, R. André, and B. Deveaud-Plédran, *Phys. Rev. Lett.* **107**, 106401 (2011).
- [13] P. Cristofolini, A. Dreismann, G. Christmann, G. Franchetti, N. G. Berloff, P. Tsotsis, Z. Hatzopoulos, P. G. Savvidis, and J. J. Baumberg, *Phys. Rev. Lett.* **110**, 186403 (2013).
- [14] A. Dreismann, P. Cristofolini, R. Balili, G. Christmann, F. Pinsker, N. G. Berloff, Z. Hatzopoulos, P. G. Savvidis, and J. J. Baumberg, *Proc. Natl. Acad. Sci. USA* **111**, 8770 (2014).
- [15] V. K. Kalevich, M. M. Afanasiev, V. A. Lukoshkin, K. V. Kavokin, S. I. Tsintzos, P. G. Savvidis, and A. V. Kavokin, *J. Appl. Phys.* **115**, 094304 (2014).
- [16] H. Ohadi, R. L. Gregory, T. Freearge, Y. G. Rubo, A. V. Kavokin, and P. G. Lagoudakis, *arXiv:1406.6377v2*.
- [17] J. Schmutzler, P. Lewandowski, M. Amann, D. Niemietz, S. Schumacher, M. Kamp, C. Schneider, S. Höfling, and M. Bayer, *Phys. Rev. B* **91**, 195308 (2015).
- [18] T. Byrnes, N. Y. Kim, and Y. Yamamoto, *Nat. Phys.* **10**, 803 (2014).
- [19] S. S. Demirchyan, I. Y. Chestnov, A. P. Alodjants, M. M. Glazov, and A. V. Kavokin, *Phys. Rev. Lett.* **112**, 196403 (2014).
- [20] D. Sanvitto, A. Amo, L. Viña, R. André, D. Solnyshkov, and G. Malpuech, *Phys. Rev. B* **80**, 045301 (2009).

- [21] M. Maragkou, A. J. D. Grundy, E. Wertz, A. Lemaître, I. Sagnes, P. Senellart, J. Bloch, and P. G. Lagoudakis, *Phys. Rev. B* **81**, 081307(R) (2010).
- [22] G. Nardin, Y. Léger, B. Pietka, F. Morier-Genoud, and B. Deveaud-Plédran, *Phys. Rev. B* **82**, 045304 (2010).
- [23] P. R. Eastham, *Phys. Rev. B* **78**, 035319 (2008).
- [24] S. Portolan, P. Hauke, and V. Savona, *Phys. Status Solidi B* **245**, 1089 (2008).
- [25] P. Tsotsis, P. S. Eldridge, T. Gao, S. I. Tsintzos, Z. Hatzopoulos, and P. G. Savvidis, *New J. Phys.* **14**, 023060 (2012).
- [26] See Supplemental Material at <http://link.aps.org/supplemental/10.1103/PhysRevB.92.035305>, for a more detailed discussion of the excitation profile and energy landscape, the calculation of the reservoir–wave-function overlap, and further details of the theoretical model simulation.
- [27] M. Wouters and I. Carusotto, *Phys. Rev. Lett.* **99**, 140402 (2007).
- [28] J. Keeling and N. G. Berloff, *Phys. Rev. Lett.* **100**, 250401 (2008).
- [29] M. Wouters, *New J. Phys.* **14**, 075020 (2012).
- [30] M. Wouters, T. C. H. Liew, and V. Savona, *Phys. Rev. B* **82**, 245315 (2010).
- [31] E. Wertz, A. Amo, D. D. Solnyshkov, L. Ferrier, T. C. H. Liew, D. Sanvitto, P. Senellart, I. Sagnes, A. Lemaître, A. V. Kavokin, G. Malpuech, and J. Bloch, *Phys. Rev. Lett.* **109**, 216404 (2012).
- [32] C. Antón, T. C. H. Liew, G. Tosi, M. D. Martín, T. Gao, Z. Hatzopoulos, P. S. Eldridge, P. G. Savvidis, and L. Via, *Appl. Phys. Lett.* **101**, 261116 (2012).
- [33] D. D. Solnyshkov, H. Terças, K. Dini, and G. Malpuech, *Phys. Rev. A* **89**, 033626 (2014).
- [34] L. M. Sieberer, S. D. Huber, E. Altman, and S. Diehl, *Phys. Rev. B* **89**, 134310 (2014).
- [35] H. Haug, T. D. Doan, and D. B. Tran Thoai, *Phys. Rev. B* **89**, 155302 (2014).
- [36] We used the following parameters to describe our system:  $m_p = 7 \times 10^{-5} m_e$ ,  $U_{\text{pol-pol}} = 2.4 \times 10^{-3} \text{ meV } \mu\text{m}^2$ ,  $U_{\text{pol-ex}} = 2U_{\text{pol-pol}}$ ,  $\Gamma_{\text{NL}} = 0.3U_{\text{pol-pol}}$  [28],  $r = 6 \times 10^{-4} \text{ meV } \mu\text{m}^2$ ,  $\lambda = 1.2 \times 10^{-3} \mu\text{m}^2\text{ps}^{-1}\text{meV}^{-1}$ ,  $\hbar/\Gamma = 5 \text{ ps}$ .
- [37] M. Combescot and D. W. Snoke, *Phys. Rev. B* **78**, 144303 (2008).
- [38] B. Nelsen, G. Liu, M. Steger, D. W. Snoke, R. Balili, K. West, and L. Pfeiffer, *Phys. Rev. X* **3**, 041015 (2013).
- [39] T. C. H. Liew, M. M. Glazov, K. V. Kavokin, I. A. Shelykh, M. A. Kaliteevski, and A. V. Kavokin, *Phys. Rev. Lett.* **110**, 047402 (2013).
- [40] H. S. Nguyen, D. Vishnevsky, C. Sturm, D. Tanese, D. Solnyshkov, E. Galopin, A. Lemaître, I. Sagnes, A. Amo, G. Malpuech, and J. Bloch, *Phys. Rev. Lett.* **110**, 236601 (2013).

# Supplementary Information: A robust platform for engineering pure-quantum-state transitions in polariton condensates

## S1 Excitation and energy landscape

The trap profile can be directly visualised by imaging the photoluminescence of the sample prior to the onset of condensation. Figure S1 depicts the emission below and above threshold for six condensed states where the excitation has been filtered out with the use of a high pass filter. It is worth pointing out that the laser intensity is not uniform throughout the excitation region and this will result in a non-uniform height of the trap barrier. The bound states of such a trapping potential will thus be defined by the lowest energy of the trapping barrier at condensation threshold. Figures S1a-c show the trap profile below threshold and the emission above threshold for the  $\Psi_{03}$ ,  $\Psi_{05}$  and  $\Psi_{12}$  states respectively, while figures S1d-f depict additional higher order asymmetric states formed when increasing the trap size. It is worth pointing out that the spatial patterns above threshold are shown to consistently form always inside the excitation region.

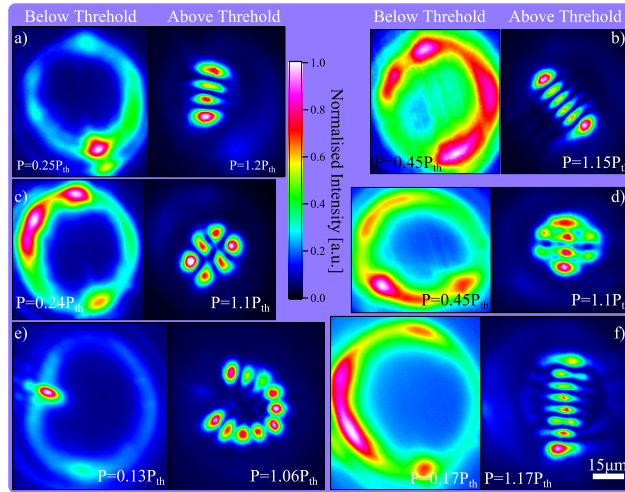


Figure S1: Emission below (left) and above threshold (right) for different trap configurations resulting in condensation in the  $\Psi_{03}$  a),  $\Psi_{05}$  b) and  $\Psi_{12}$  c) and for highly asymmetric states formed for larger traps with a total number of 8, 10 and 11 lobes d), e) and f) respectively.

The potential landscape in the region of the pump is expected to follow the intensity profile of the excitation. This can be directly imaged by spectrally resolving a narrow slice of the real space emission. Figure S2a) shows the energy resolved emission below (left) and above (right) threshold for the  $\Psi_{01}$  state of fig.1b of the main text. Above threshold we observe the doublet state on a single energy level, while below threshold the parabolic profile of the trap is seen. In figures S2b,c the energy resolved emission below and above threshold is displayed for the states corresponding to S1d,f respectively and figS1d is for the energy resolved experiment of figure 3 of the main text.

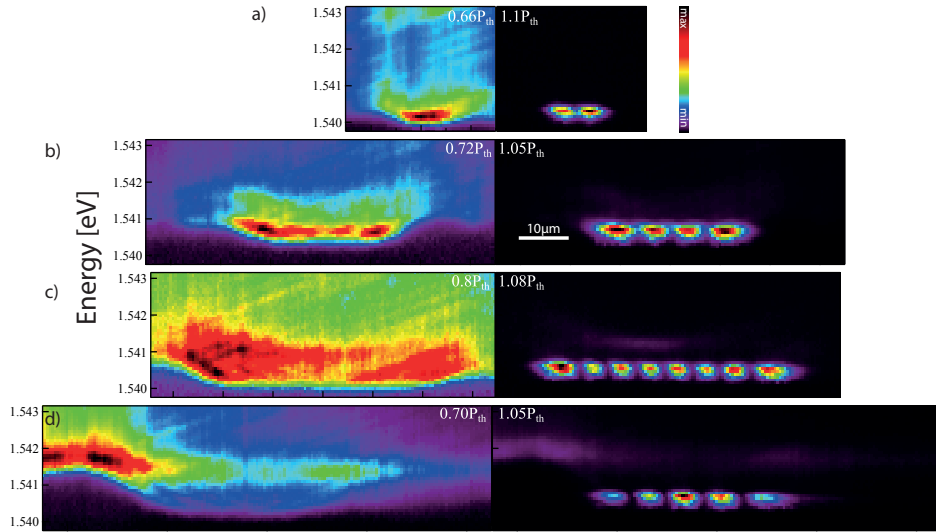


Figure S2: Energy resolved photoluminescence below and above threshold for  $\Psi_{01}$  (a),  $\Psi_{03}$  (b) for the spatial pattern of S1f) (c) and for  $\Psi_{04}$  of figure 3 of the main text (d).

These images clearly illustrate the shape of the energy landscape prior to condensation, where the energy at the excitation region is considerably blue-shifted compared to the energy level in the centre. However, it must be noted that as previous studies have shown [1], polariton particles in the barrier are greatly out of equilibrium, have increased kinetic energies and do not efficiently populate the ground state of the dispersion. Therefore the energy profile outlined by the emission in S2a-d is actually deeper than the actual one. The real energy profile of the trap can only be intermediately reconstructed by filtered dispersion imaging along neighbouring points on the X axis and then each dispersion fitted with a polariton dispersion in order to find the  $k_x=0$  level along X. However a measurement of this sort would entail a substantial error margin due to the broadening of the momentum space in spatially filtered measurements due to the uncertainty principle.

## S2 One dimensional model and reservoir wavefunction overlap

It is straightforward to implement a 1D model of the trap and numerically solve the Schrödinger equation for the experimentally calculated polariton mass ( $m_p = 4.5 \times 10^{-5} m_e$ ). We approximate the profile of the trap by 2 Gaussian beams at a distance equal to the trap diameter and a FWHM of  $\sim 10 \mu\text{m}$ . Increasing the radius of the trap inevitably modulates the energy levels of the available trapped states. Intuitively for large trap sizes the bound states closely match those of a square well potential with a parabolic energy-mode dispersion, while for smaller optical traps the trap profile is increasingly parabolic, featuring a linear energy-mode dispersion. Figure S3a shows the calculated energy levels of the 1D trap for increasing trap radius. Under the simplification that the barrier height (blue-shift) would remain constant it is evident that the highest energy level, where we expect condensation to occur, doesn't have a monotonic dependence on the size of the trap. It is worth pointing out the remarkable quantitative agreement of this model, regarding the energy difference of the fourth and fifth excited states for a trap radius of the order of  $20 \mu\text{m}$ , with the experimentally measured value of  $\approx 45 \mu\text{eV}$ .

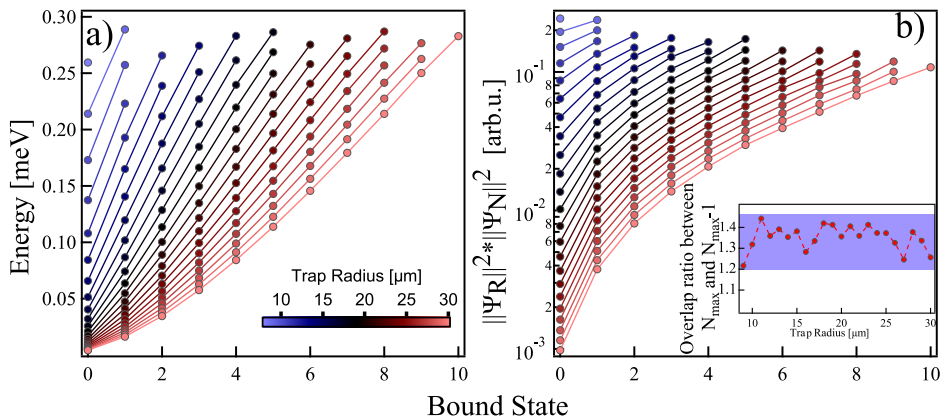


Figure S3: **Energy levels and corresponding wavefunction reservoir overlap for different trap radii.** **a)** Calculated energy levels for increasing trap radius for a trap depth of 0.3 meV for a numerical simulation as described in the text **b)** Corresponding calculated overlap of bound states with the trap barriers (reservoir). Inset in b), overlap ratio of  $N=\text{Max}$  and  $N=\text{max}-1$  vs trap radius.

As stated in the manuscript, intuitively the overlap of the bound wavefunctions is greater for the higher order modes for each trap configuration. Quantifying the overlap of the wavefunction with the reservoir as the area of the product of  $|\langle\Psi_N\rangle|^2$  with  $|\langle\Psi_R\rangle|^2$  we are able to compare the overlap of the calculated energy levels of fig. S3a. Figure S3b graphically depicts this calculation showing that indeed the overlap follows a monotonic dependence for increasing  $N$ , for each trap configuration (radius). It is noteworthy that the overlap ratio between the highest 2 states in the trap ranges from 1.2 to 1.45 for the range of the calculation. This shows that the injection of particles to the highest energy

state depending on the individual trap configuration can be up to 45% more efficient than to the next available energy state (inset in [S3b](#)).

### S3 Theoretical model

The pump profile including exciton diffusion was taken as:

$$f_r(\mathbf{r}) = \frac{L_0^4}{\left((x^2 + \beta y^2 - r_0^2)^2 + L_0^4\right)} \quad (1)$$

where  $L_0$  determines the thickness of the ring,  $\beta$  is related to the ellipticity, and  $r_0$  is the radius. In order to define the chemical potential, we follow a similar technique to ref. [\[2\]](#). The energy relaxation term has the form:

$$\Re[\psi(\mathbf{r}, t)] = -\lambda N_r f_r(\mathbf{r}) \left(\hat{E}_{\text{LP}} - \mu(\mathbf{r}, t)\right) \psi(\mathbf{r}, t) \quad (2)$$

$$= \left. \frac{d\psi(\mathbf{r}, t)}{dt} \right|_{\Re} \quad (3)$$

where the notation used in the last line indicates that this is the contribution to  $d\psi(\mathbf{r}, t)/dt$  due to energy relaxation. The local effective chemical potential  $\mu(\mathbf{r}, t)$  is defined to enforce the condition that energy relaxation does not change the total polariton density,  $n(\mathbf{r}, t)$ :

$$\left. \frac{d\sqrt{n(\mathbf{r}, t)}}{dt} \right|_{\Re} = 0 \quad (4)$$

Note, however, that other terms in  $d\psi(\mathbf{r}, t)/dt$  may change the polariton density (e.g., pumping and decay terms). The polariton density is related to the wavefunction by  $\psi(\mathbf{r}, t) = \sqrt{n(\mathbf{r}, t)}e^{i\theta(\mathbf{r}, t)}$ , where  $\theta(\mathbf{r}, t)$  is the local condensate phase. Note that:

$$\begin{aligned} \left. \frac{d\psi(\mathbf{r}, t)}{dt} \right|_{\Re} &= \left. \frac{d\sqrt{n(\mathbf{r}, t)}}{dt} \right|_{\Re} e^{i\theta(\mathbf{r}, t)} \\ &\quad + i\sqrt{n(\mathbf{r}, t)}e^{i\theta(\mathbf{r}, t)} \left. \frac{d\theta(\mathbf{r}, t)}{dt} \right|_{\Re} \end{aligned} \quad (5)$$

Multiplying by  $e^{-i\theta(\mathbf{r}, t)}$  and taking the real parts, we find that:

$$\Re \left\{ \left. \frac{d\psi(\mathbf{r}, t)}{dt} \right|_{\Re} e^{-i\theta(\mathbf{r}, t)} \right\} \quad (6)$$

$$= \Re \left\{ \Re[\psi(\mathbf{r}, t)] e^{-i\theta(\mathbf{r}, t)} \right\} \quad (7)$$

$$= \Re \left\{ -\lambda N_r f_r(\mathbf{r}) \hat{E}_{\text{LP}} \psi(\mathbf{r}, t) e^{-i\theta(\mathbf{r}, t)} \right\} \quad (8)$$

$$+ \Re \left\{ \lambda N_r f_r(\mathbf{r}) \mu(\mathbf{r}, t) \psi(\mathbf{r}, t) e^{-i\theta(\mathbf{r}, t)} \right\} \quad (9)$$

$$= \left. \frac{d\sqrt{n(\mathbf{r}, t)}}{dt} \right|_{\Re} \quad (10)$$

According to condition 4, this term must vanish. This is precisely the condition enforced by the chemical potential  $\mu(\mathbf{r}, t)$ . This leaves only the imaginary part non-zero:

$$\begin{aligned} \Re[\psi(\mathbf{r}, t)]e^{-i\theta(\mathbf{r}, t)} &= i\text{Im}\left\{\Re[\psi(\mathbf{r}, t)]e^{-i\theta(\mathbf{r}, t)}\right\} \end{aligned} \quad (11)$$

$$= i\text{Im}\left\{-\lambda N_r f_r(\mathbf{r})\hat{E}_{\text{LP}}\psi(\mathbf{r}, t)e^{-i\theta(\mathbf{r}, t)}\right\} \quad (12)$$

or

$$\Re[\psi(\mathbf{r}, t)] = ie^{-i\theta(\mathbf{r}, t)}\text{Im}\left\{-\lambda N_r f_r(\mathbf{r})\hat{E}_{\text{LP}}\psi(\mathbf{r}, t)e^{-i\theta(\mathbf{r}, t)}\right\} \quad (13)$$

This shows that in practice we do not need the explicit form of  $\mu(\mathbf{r}, t)$  as the above expression can be used in the evolution equation for the polariton wavefunction.

## References

- [1] Askitopoulos, A., Ohadi, H., Kavokin, A. V., Hatzopoulos, Z., Savvidis, P. G., and Lagoudakis, P. G. *Physical Review B* **88**(4), 041308 July (2013).
- [2] Wouters, M., Liew, T. C. H., and Savona, V. *Physical Review B* **82**(24), 245315 December (2010).